Modal approach based on global stereocorrelation for defects measurement in wire-laser additive manufacturing

Khalil Hachem, Yann Quinsat, Christophe Tournier, Nicolas Béraud

Modal approach based on global stereocorrelation for defects measurement in wire-laser additive manufacturing

Khalil Hachem[a,*], **Yann Quinsat**[a], **Christophe Tournier**[a], **Nicolas Béraud**[b]
[a] *Université Paris-Saclay, ENS Paris-Saclay, LURPA, Gif-sur-Yvette, France, 91190*
[b] *Univ. Grenoble Alpes, CNRS, Grenoble INP, G-SCOP, Grenoble, France, 38000*

Abstract. Producing near net shape parts with complex geometries using wire-laser additive manufacturing (AM) often requires a mastered and optimized process. Differences between the constructed and nominal geometries of the manufactured entities demand an *in-situ* defects measurement to complete the production of the entire part successfully. A contactless measuring system is needed to evaluate geometrical deviations without requiring complex post-processing operations. To overcome this challenge and validate a measuring tool that serves the manufacturing purpose, a global stereocorrelation approach is used to measure defects in wire-laser additively manufactured parts. This method relies on the cameras' self-calibration phase that uses the part substrate's nominal model. Then, a modal basis is defined to model and evaluate the surface dimensional and shape defects. Hence, an analysis of the texture obtained in AM is conducted to assess whether or not it is sufficient for image correlation and defect measurement. Finally, natural and pattern textures are compared to highlight their influence on the measurement results.

Keywords: wire-laser additive manufacturing; image correlation; defects measurement; modal basis; texture analysis.

*Address all correspondence to Khalil Hachem, khalil.hachem@ens-paris-saclay.fr

1 Introduction

A new industrial manufacturing era started with the evolution of additive manufacturing (AM). This process entered high levels of industry and production. Its advantage over the subtractive techniques is producing parts with complex internal and external features[1] and repairing damaged parts.[2] Wire-laser additive manufacturing (WLAM) is a branch of AM processes where a stream of metal wire is delivered to a substrate in order to intersect with a concentrated laser energy source at a common focal point, forming a melt pool and depositing material layer by layer. The corresponding machine includes a laser system and an automated wire feed supply unit moved by an operated robot arm. The machine worktable can achieve rotary substratum movement, and some accessory devices, such as gas shielding, are necessary. Additively manufactured parts present different types of defects and deviations from the nominal design due to many factors. Equipment's improper performance can induce them, in addition to the configuration of the corresponding process parameters, the quality of the feedstock material, and the heat accumulation in the produced part.[3–5] Therefore, on a larger scale, defects classifications exist for directed energy deposition (DED) processes, including the wire-laser one. According to Liu *et al.*,[6] part quality and defects affecting DED parts can be classified into three categories: geometrical (form and dimensions),

morphological (surface texture), and microstructural anomalies. Therefore, at both layers and entity levels, defects in WLAM can be seen and treated as internal (microstructural non-homogeneity, porosity, etc.) and external (geometrical, edge defects, waviness, surface roughness, etc.). In the following, this paper highlights external defects, more precisely geometrical ones, where dimensional and shape deviations can be found.

Complex geometries in AM often require more than one deposition sequence. The part can be built through many stages while changing its position and orientation between phases. Consequently, differences between the produced and nominal geometries can penalize the ongoing and upcoming process. These defects can be seen at the entity level as geometrical positioning and orientation deviations or at the surface level as material gaps on the final parts, blobs, and zits. All these can risk collisions between the effector and the part, disturb the additive trajectories, and pile up defects through the end of the process. That is why it is necessary to measure these deviations *in-situ* to update the additive trajectories with regard to the occurring geometrical defects. A contactless measuring system is mandatory to evaluate geometrical defects without requiring complex post-processing operations. It also helps to achieve *in-situ* measurements without interrupting the process or removing the part from its manufacturing environment. Hence, optical signal-based detection with its spatially resolved charge-coupled device/complementary metal oxide semiconductor (CMOS) cameras is becoming more popular, especially with the evolution of the image correlation technique.[1] Its capability to provide full field measurements with a direct evaluation of the part deformation is valuable and efficient in shape measurement.[7] Rebergue *et al.*[8] and Dubreuil[9] achieved *in-situ* measurements during machining using digital image correlation (DIC). In contrast, Dufour[10] used this technique to measure three-dimensional (3D) displacement fields with a numerical description of the analyzed surfaces (non-uniform rational B-splines known as NURBS).

Modal decomposition, based on free vibrational modes, proved its relevance for form defect analysis and was used in different previous works, having the same objective of identifying and expressing shape deviations of thin parts[11] and medium-sized machined surfaces.[7] More precisely, shape defect is decomposed of several elementary participations, whose sum best fits the observed defects. Building upon this, Etievant *et al.*[7] developed a modal approach for shape defect measurement based on global stereocorrelation. Their work includes a self-calibration phase where the measured object is used as a calibration artifact.[12,13] The nominal description of the part is defined as a triangular mesh and a speckle pattern is projected on the machined surface to texture it. This step is followed by global DIC measurement and defects evaluation using a predefined modal basis.

This proposed contribution aims to use the preceding presented approach to measure the shape and dimensional defects of parts produced by the WLAM process. Therefore, by introducing the

DIC modal approach to an AM context, the surface texture became a new variable that needs to be assessed. Unlike machined surfaces, it is a natural pattern that may influence the image correlation analysis over a region of interest (ROI). While conducting DIC measurements, the projected or painted pattern applied to the surface has a significant influence on the accuracy and precision of the results.[14–16] Moreover, the measurements are impossible without applying an appropriate pattern when dealing with non-patterned textures, such as machined surfaces. Given this perspective, this presented contribution studies the performance of the AM natural texture and its capacity to provide the needed measurement results. In consequence, a study comparing results obtained with natural and classic projected patterns is proposed to know whether the manufactured part texture is enough to exclude any added pattern. Finally, AM surfaces presenting remarkable defects question their use as targets in the self-calibration procedures and shift the attention to well-defined geometries from the manufacturing environment, such as the part's substrate.

This paper is structured as follows: the adopted modal approach and its image correlation measurement principles are presented in Sec. 2. Then, the followed experimental protocol is described in Sec. 3. Section 4 details the defects measurement and modeling of a case study along with the analysis of the results. The findings and perspectives of this research work are finally summarized in Sec. 5.

2 Measurement approach

In this work, the shape defects of an AM part are measured by global stereocorrelation. Therefore, calibrating the cameras is fundamental here, especially in an AM context where the surface texture and geometrical deviations cannot be neglected. In addition to the optical measurements, this study uses a modal approach to express the geometric deviations. In this section, the camera model is presented alongside the self-calibration technique. Then, the shape correction method is addressed, and analysis criteria are defined for the texture comparison.

2.1 Camera model and calibration

The pinhole camera model is the most specialized and simplest one. It describes the process of image formation within a camera to express the relationship between the 3D coordinates of a point in space $\left[\mathbf{X} = (X, Y, Z)\right]$, and its corresponding pixel coordinates in the image plane $\left[\mathbf{x} = (u, v)\right]$. A total of six unknowns, three rotation parameters, and three distances are essential to define the rigid transformation between the space and camera frame [Eq. (1)]. They are referred to as extrinsic parameters ($\mathbf{a}$)

$$\begin{bmatrix} X_c \\ Y_c \\ Z_c \\ 1 \end{bmatrix}_{R_{Camera}} = \begin{bmatrix} \mathbf{R_{3\times 3}} & \mathbf{t}_{3\times 1} \\ \mathbf{0}_{1\times 3} & 1 \end{bmatrix} \begin{bmatrix} X \\ Y \\ Z \\ 1 \end{bmatrix}_{R_{Space}} = \begin{bmatrix} r_{11} & r_{12} & r_{13} & t_1 \\ r_{21} & r_{22} & r_{23} & t_2 \\ r_{31} & r_{32} & r_{33} & t_3 \\ 0 & 0 & 0 & 1 \end{bmatrix} \begin{bmatrix} X \\ Y \\ Z \\ 1 \end{bmatrix}_{R_{Space}} . \tag{1}$$

Once in the camera coordinate frame, the point projection in the image plane is defined in Eq. (2) by the following intrinsic parameters: the focal length f_u, f_v expressed in pixels (width and height), the coordinates of the optical center projection: C_{cu}, C_{cv}, and the skew factor s_k

$$\begin{bmatrix} u \\ v \\ 1 \end{bmatrix}_{R_{Image}} = \begin{bmatrix} f_u & s_k & C_{cu} & 0 \\ 0 & f_v & C_{cv} & 0 \\ 0 & 0 & 1 & 0 \end{bmatrix} \begin{bmatrix} X_c \\ Y_c \\ Z_c \\ 1 \end{bmatrix}_{R_{Camera}} . \tag{2}$$

Finally, image distortions are computed and taken into consideration.[17] A projection matrix $[\mathbf{P}]_{(3\times 4)}$ containing both intrinsic and extrinsic parameters is defined as

$$\mathbf{P} = \underbrace{\begin{bmatrix} f_u & s_k & C_{cu} & 0 \\ 0 & f_v & C_{cv} & 0 \\ 0 & 0 & 1 & 0 \end{bmatrix}}_{\text{Intrinsic } (3\times 4)} . \underbrace{\begin{bmatrix} \mathbf{R_{3\times 3}} & \mathbf{t}_{3\times 1} \\ \mathbf{0}_{1\times 3} & 1 \end{bmatrix}}_{\text{Extrinsic } (4\times 4)} . \tag{3}$$

From a distortion-corrected image, it is possible to obtain the relationship between $\mathbf{X}$ and $\mathbf{x}$ using $[\mathbf{P}]$ and a scale factor s as follows:

$$s. \begin{bmatrix} u \\ v \\ 1 \end{bmatrix}_{R_{Image}} = [\mathbf{P}] \begin{bmatrix} X \\ Y \\ Z \\ 1 \end{bmatrix}_{R_{Space}} \rightarrow s.\mathbf{x} = [\mathbf{P}]_{(3\times 4)}.\mathbf{X}. \tag{4}$$

Equation (5) details the relation between the space and image points function of the projection matrix parameters

$$\begin{aligned} u &= \frac{\mathbf{P_{11}}X + \mathbf{P_{12}}Y + \mathbf{P_{13}}Z + \mathbf{P_{14}}}{\mathbf{P_{31}}X + \mathbf{P_{32}}Y + \mathbf{P_{33}}Z + \mathbf{P_{34}}} \\ v &= \frac{\mathbf{P_{21}}X + \mathbf{P_{22}}Y + \mathbf{P_{23}}Z + \mathbf{P_{24}}}{\mathbf{P_{31}}X + \mathbf{P_{32}}Y + \mathbf{P_{33}}Z + \mathbf{P_{34}}}. \end{aligned} \tag{5}$$

2.2 *Calibration of stereoscopic system*

Calibrating a stereoscopic system (with at least two cameras) is about determining the projection matrix of each camera according to the same reference frame. Different calibrating methods and classical techniques exist.[18,19] Most of these methods are based on extracting geometric elements (points or lines) whose relative position is known. For this purpose, artifacts of known geometry are generally used. These objects are made up of remarkable points, such as the intersection of vertical and horizontal horizontal lines (checkerboards) or the center of elliptical spots. Two types of calibration patterns are commonly used to calibrate stereovision systems: plane patterns and 3D patterns.

Recent works propose a self-calibration method using the same images for calibration and measurement. This approach requires a mathematical description of the analyzed surface, whether NURBS patches[12] or triangular meshes.[7,13] The main objective is to determine the left and right camera calibration matrices such that the 3D numerical model of the object is best projected on both images. First, this 3D model $\mathbf{X_0}$ is projected on left and right images using fixed intrinsic and random extrinsic parameters. Then, the extrinsic parameters are changed manually to have the model's best initial image projections $\mathbf{x_0}$. Subsequently, these manual estimations of the 2D points determine the initial projection matrices [Eq. (4)]. Then, in the second step, an underlying minimization principle is used. It is based on the gray level conservation in the acquired images [Eq. (6)]. The functions f^l and f^r represent the pixel intensities (gray levels) of the left and right images, respectively, at positions $\mathbf{x^l}$ and $\mathbf{x^r}$. These positions correspond to the projection of the same 3D point $\mathbf{X}$ onto both images' planes

$$f^l(\mathbf{x^l}) = f^r(\mathbf{x^r}). \tag{6}$$

However, this conservation is only valid if the exact value of the calibration parameters (i.e., the two projection matrices) are well known and there is no noise during the acquisition. In practice, this is not the case. A global formulation of the problem is necessary in which the sum of the least squares is expressed in the parametric space in the form of an image correlation residual $\mathcal{T}$ shown as

$$\mathcal{T} = \sum_{ROI} \Big(f^l\big(\mathbf{x^l}(\mathbf{X_0}, [\mathbf{P}^l])\big) - f^r\big(\mathbf{x^r}(\mathbf{X_0}, [\mathbf{P}^r])\big) \Big)^2. \tag{7}$$

Hence, the correlation residual $\mathcal{T}$ expresses the gray level difference between the pixels of the two images. It is minimized with respect to the left $[\mathbf{P}^l]$ and right $[\mathbf{P}^r]$ projection matrices over the entire ROI. The 2D projections of the nominal 3D model define the studied areas in the images, also called ROI. Hence, an optimized projection matrix leads to lower residual $\mathcal{T}$. As

a result, the optimal solution of these matrices is determined; therefore, the stereoscopic system calibration.[7] As in a standard global approach, the Gauss-Newton method minimizes the sum of squared differences. For this purpose, this sum is linearized in Eq. (8) where the image gradient is represented by ∇f

$$\mathcal{T}_{lin}(\mathrm{d}\mathbf{P}^l, \mathrm{d}\mathbf{P}^r) = \sum_{ROI} \Big(f^l(\mathbf{x^l}) - f^r(\mathbf{x^r}) + (\nabla f^l . \delta\mathbf{x^l})(\mathbf{x^l}) - (\nabla f^r . \delta\mathbf{x^r})(\mathbf{x^r}) \Big)^2. \tag{8}$$

The evolution of the calibration parameters values $\mathrm{d}\mathbf{P}^{l,r}$ allows adjusting the coordinates of the projections of each 3D point on the left and right images ($\delta\mathbf{x^{l,r}} = \frac{\partial \mathbf{x^{l,r}}}{\partial \mathbf{P}^{l,r}} \mathrm{d}\mathbf{P}^{l,r}$).

While optimizing the projection matrices, 24 unknowns are computed. This problem can be simplified for better results by determining the calibration parameters separately. The intrinsic ones are found and fixed using a calibration target. In contrast, extrinsic ones are now computed, which reduces the problem to 12 unknowns (six parameters for each camera).[20] The new linarized relation is shown in Eq. (9) (with $\delta\mathbf{x^{l,r}} = \frac{\partial \mathbf{x^{l,r}}}{\partial \mathbf{P}^{l,r}} \frac{\partial \mathbf{P}^{l,r}}{\partial \mathbf{a^{l,r}}} \mathrm{d}\mathbf{a}^{l,r}$)

$$\mathcal{T}_{lin}(\mathrm{d}\mathbf{a^l}, \mathrm{d}\mathbf{a^r}) = \sum_{ROI} \Big(f^l(\mathbf{x^l}) - f^r(\mathbf{x^r}) + (\nabla f^l . \delta\mathbf{x^l})(\mathbf{x^l}) - (\nabla f^r . \delta\mathbf{x^r})(\mathbf{x^r}) \Big)^2. \tag{9}$$

*2.3 **Shape measurement and correction***

Once the calibration is performed, the nominal surface is deformed using a defect database obtained by modal analysis. The corresponding modes of this basis are generated using computed aided design (CAD) software. Hence, the estimate of the modal deformation $\mathbf{X}$ is computed by starting with the nominal position vector $\mathbf{X_0}$ [Eq. (10)] and adding to it the corresponding displacement that best expresses the present shape defect. Λ_i are the modal amplitudes associated with the N modes $\mathbf{q_i}$

$$\mathbf{X} = \mathbf{X_0} + \sum_{i=1}^{N} \Lambda_i . \mathbf{q_i}, \tag{10}$$

$$\{\mathbf{\Lambda_{opt}}\} = \underset{\{\mathbf{\Lambda}\}}{argmin} \sum_{ROI} \Big(f^l\big([\mathbf{P^l}](\mathbf{X})\big) - f^r\big([\mathbf{P^r}](\mathbf{X})\big) \Big)^2. \tag{11}$$

The deformation of the projected 3D model reduces the differences between the images' pixel intensities. Hence, in Eq. (11), the corresponding modal amplitudes are determined to minimize this global correlation residual over the measured ROI. The linear problem is solved in the same way as in Eq. (9). A Gauss-Newton algorithm is implemented where the minimization procedure stops once the corrections to the estimated modal amplitudes are very low. This explains the need

for a higher image gradient for faster convergence. The modal basis is projected according to the normal of the local surface to highlight displacements induced by shape defects.[7]

*2.4 **Image analysis***

Image correlation is an experimental technique for measuring field displacement by matching digital photos of an object. Hence, being in a new manufacturing context and questioning the natural surface capabilities requires finding criteria to qualify the images before the measurements and comparing the different textures.

First, an image gradient (∇f) describes the intensity change in an image. It characterizes the contrast of an image by providing information about the spatial variations of pixel values in different directions. It is defined by a 2D vector with components given by the derivatives in the horizontal G_x and vertical G_y directions. Moreover, it's a crucial element in the linearized optimization problems of this study. Given this perspective, an average gradient (AG) is computed [Eq. (12)],[21] where $H \times W$ is the size of the image (its height and width expressed in pixels)

$$AG = \frac{1}{(H-1)(W-1)} \sum_x \sum_y \frac{\sqrt{G_x^2 + G_y^2}}{\sqrt{2}}. \tag{12}$$

When dealing with DIC optimization problems, the aim is to reduce the gray level differences between the images, and the gradient offers insight into the direction of the steepest ascent or descent. Should there be a significant gradient at a particular point, it suggests a steep slope in the optimization. By leveraging gradient information, algorithms can accelerate convergence and rapidly achieve results. Hence, a better AG allows faster convergence of the correlation residual.

On the other hand, spatial autocorrelation refers to the presence of a spatial variation in the mapped variable. This criterion is computed in Eq. (13), where σ is the standard deviation (STD)

$$C(\delta) = \frac{\overline{f(\mathbf{x}) f(\mathbf{x}+\delta)} - \overline{f(\mathbf{x})}^2}{\sigma^2(f)}. \tag{13}$$

The output is the normalized correlation $(-1 < C < 1)$; a null value is the perfect case, while $C > 0$ means that adjacent observations have similar data values. This criterion compares the image with itself but with a displacement of pixels (δ) in horizontal and vertical directions. By focusing on the surface of interest, the mapping results inform about the sensitivity to variations. Finally, the case study in the following section lists the numerical application of these criteria.

3 Experimental protocol

In order to measure dimensional and shape defects occurring in parts produced by WLAM, an experimental protocol must be followed to reach the main objective in a structured way (Fig. 1). It

is important to note that the test part used in this work is built on a substrate having a well defined geometry. Moreover, a Canon EOS7D camera, a structured light scanning ATOS Core system, a Sony SXRD 4k pattern projection, a calibration target, CATIA, and MATLAB software are used to execute this protocol.

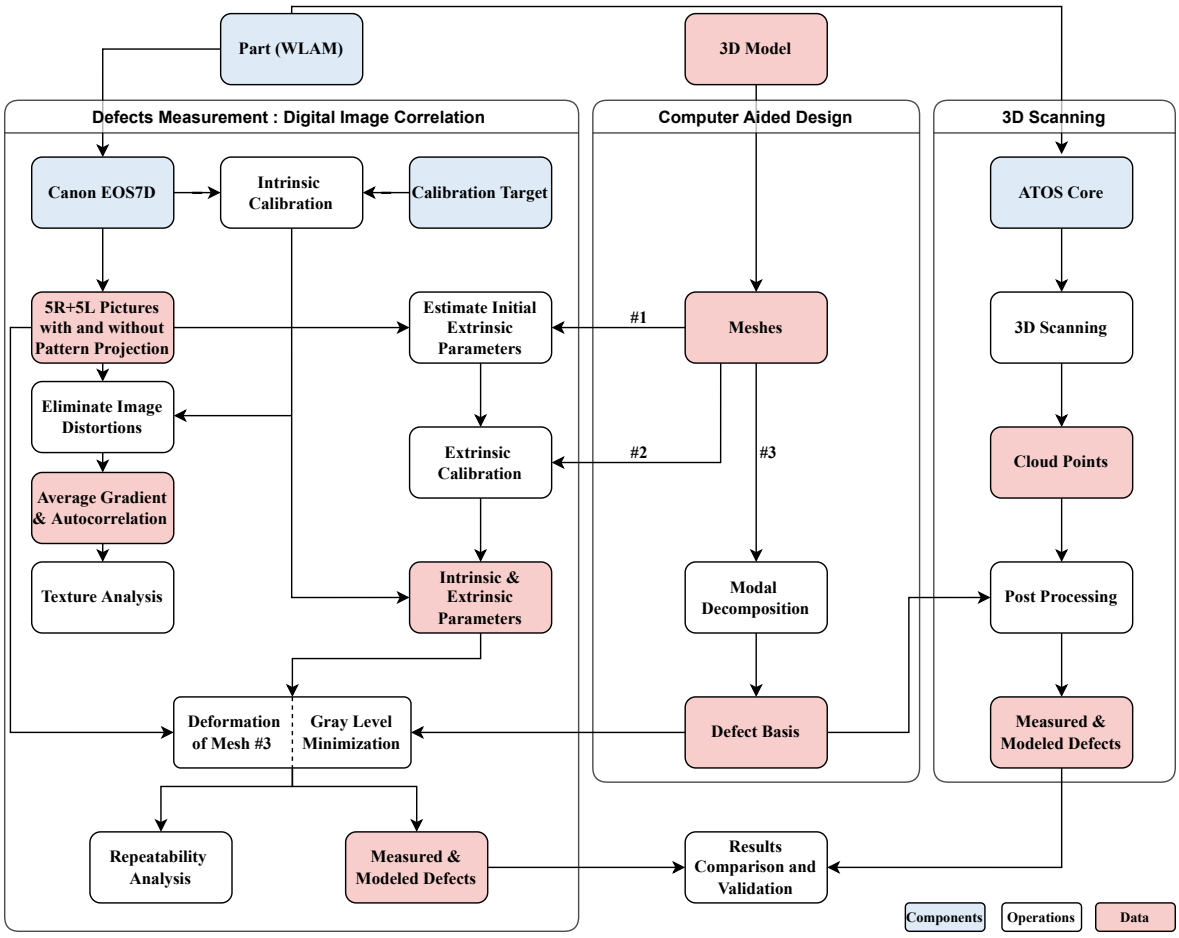

Fig 1 Flow chart of the fully adapted experimental protocol.

The CAD model of the part and the substrate are created, as well as the three meshes needed for each step of the method. Then, a modal decomposition for the third meshed surface is defined using vibrational modes. The part is scanned using the ATOS Core system to have a reference measurement and choose the defect modal basis.

After that, a calibration target is used to determine the intrinsic parameters. Therefore, the next important step is taking left and right pictures of the part with and without pattern projection. Hence, five left images and five right ones are needed to analyze the measurement results' repeatability at the end. Then, intrinsic parameters are used to eliminate image distortions, and correlation criteria (autocorrelation and AG) are computed to help analyze and compare the different textures.

Once these criteria are approved, the first mesh helps estimate initial extrinsic parameters, and the second one serves in the extrinsic self-calibration.

Once calibration parameters are separately determined (intrinsic + extrinsic), the third mesh is projected, and a phase of defects modeling, using the defined modal basis, is launched. The nominal mesh is deformed while minimizing the gray level difference between the two images. These results must be verified and validated; that is why a comparison between defects measurement obtained by the ATOS Core and the modal approach based on global stereocorrelation must be done. Finally, a repeatability analysis of the stereocorrelation measurement can then be feasible. All these steps and their results are detailed in the following section.

4 Case study

The presented study is conducted on a WLAM part to validate the use of the modal approach based on global stereocorrelation in the measurement of geometrical defects by comparing these results with another industrial measuring method. The considered part, shown in Fig. 2, is a $42.7mm \times 42.7mm$ hollow column with a height of $35mm$ centered on an $80mm \times 80mm \times 20mm$ substrate whose nominal description is defined in a CAD model. During the AM process, the deposited beads present a well-known geometry that depends on the selected process parameters. In this case, they are around $3mm$ wide and $1mm$ high, which defines the beads' scale.

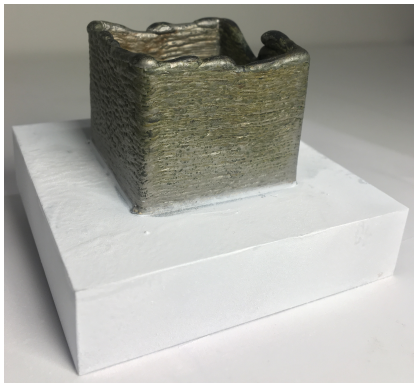

Fig 2 Part produced by wire-laser additive manufacturing.

Different surface meshes are used during the various steps of the method. They are represented by the yellow areas in Fig. 3. These meshed surfaces define the ROI and constitute the 3D points that are projected onto the images in the calibration and measurement steps. Table 1 summarizes the use of each mesh and its visualization. The first two meshes rely on the substrate surfaces, and the third one uses the AM one.

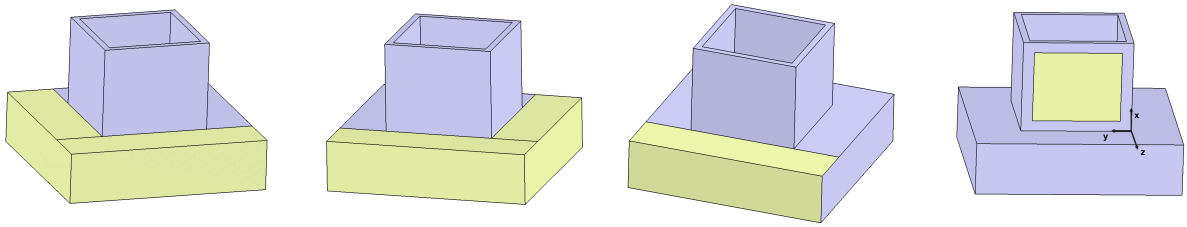

(a) (b) (c) (d)

Fig 3 (a) and (b) Surfaces used for the estimation of the initial parameters, (c) extrinsic calibration, and (d) defects measurement.

Table 1 Description of the different used meshes.

Mesh Number	**Used for**		
#1	Estimation of initial parameters	Left extrinsic parameters	Fig. 3(a)
		Right extrinsic parameters	Fig. 3(b)
#2	Extrinsic calibration		Fig. 3(c)
#3	Modal basis creation / Defects measurement		Fig. 3(d)

4.1 ***Reference measurement***

In order to validate the stereocorrelation measurement results, it is essential to estimate the geometrical defects using a reference system, in the present case, a structured light scanning device (Atos Core). This optical system efficiently measures complex shapes,[7] with low uncertainty and an STD shape error of $3\,\mu m$. Once the part is measured, a point cloud is obtained and must be processed to extract the geometrical deviations. First, the ATOS Core measurement frame is aligned with the CAD model. The substrate nominal description is used for this point cloud frame realignment. A non-rigid registration algorithm for form defect identification is implemented in the second step. This method, developed by Thiébaut *et al.*,[11] is based on a deformable iterative closest point (ICP) algorithm and a modal approach to express form defects.

A defect basis is defined using the third mesh [Fig. 3(d)]. Since the objective is to evaluate defects along the surface normal (z-axis), these rigid modes can be reduced to 3 to model dimensional deviations. The first mode represents a translation along the z-axis, while the second and third are rotations around the x- and y-axes, respectively. Geometrical deviations of the part are estimated using these 3 modes [Fig. 4(a)]. The results showed critical dimensional defects concerning the column position [Mode #1 in Fig. 4(c)] and inclination [Modes #2-3 in Fig.4(c)]. Then, the rest of the deformable modes are defined as sinusoidal functions,[11] representing shape defects. A total basis of 25 modes is used, and modes with nearly zero z-components (normal surface direction) have been eliminated. Figure 4(b) shows the geometrical defects expressed by the non-rigid body modes of the adapted basis. The following section analyzes and defines the modal basis size for

this research findings.

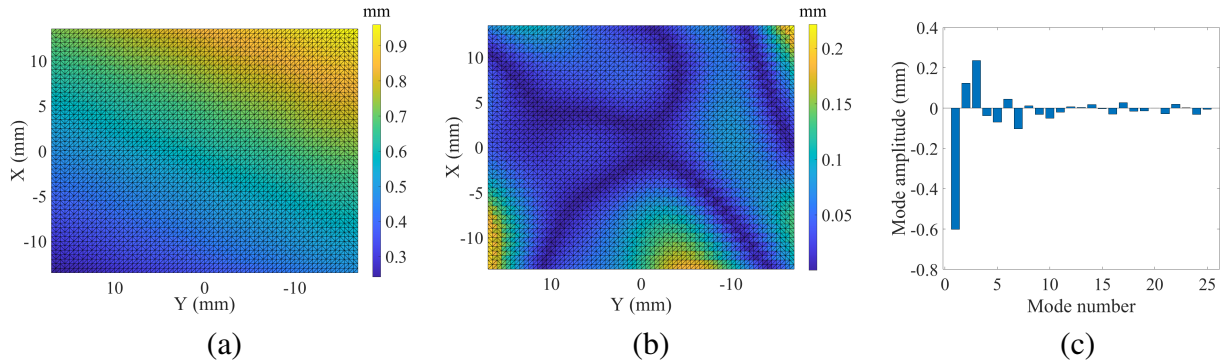

Fig 4 (a) Geometrical defects measured by three rigid body modes and (b) the following 22; (c) Modal amplitudes using ATOS Core with a modal basis of 25 modes.

4.2 ***Defect basis size***

As mentioned before, the defect basis is defined by vibrational modes. Thus, their number and the reached frequencies are essential to determine the scale of the modeled deviations. With higher frequencies, a larger modal basis is generated. Therefore, it can model deviations at a lower scale, leading to the beads one. Hence, more than 25 modes are needed, leading to the generation of around 1600 modes filtered to 850 to keep the ones representing defects along the surface normal (z-axis). Full bases going from 25 to 850 modes are used, respectively. After applying the ICP algorithms on the scanned point cloud and the nominal mesh using the modal analysis, Fig. 5 shows a residual map of this registration after the modeling, with bases having different numbers of modes. These residuals represent the difference between the scanned point cloud and the deformed nominal mesh after applying the corrections and node displacements using the modal basis. The advantage of these maps is that they compare the actual defects with those being modeled with the defined basis. The residuals of this comparison inform about the deviations not detected by the modeling.

The residuals' Root Mean Square (RMS) goes down from $0.613mm$ before the modeling to $0.053mm$ with 25 modes. Then, it decreases to $0.043mm$ with 150 modes, arriving at the end at $0.022mm$ with 850 modes. This means that using a higher number of modes with higher frequencies leads to lower deviation. Therefore, the deformed nominal mesh using the modal approach is getting closer, in the representation, to the real scanned defects. The corresponding maps clearly show the added value of having a higher number of modes. Knowing the bead geometry and the obtained surface in AM, one can expect to see the horizontal stripes in the defect maps. Figure 5(b) shows lower residuals than those obtained with 25 modes but does not represent a clear bead

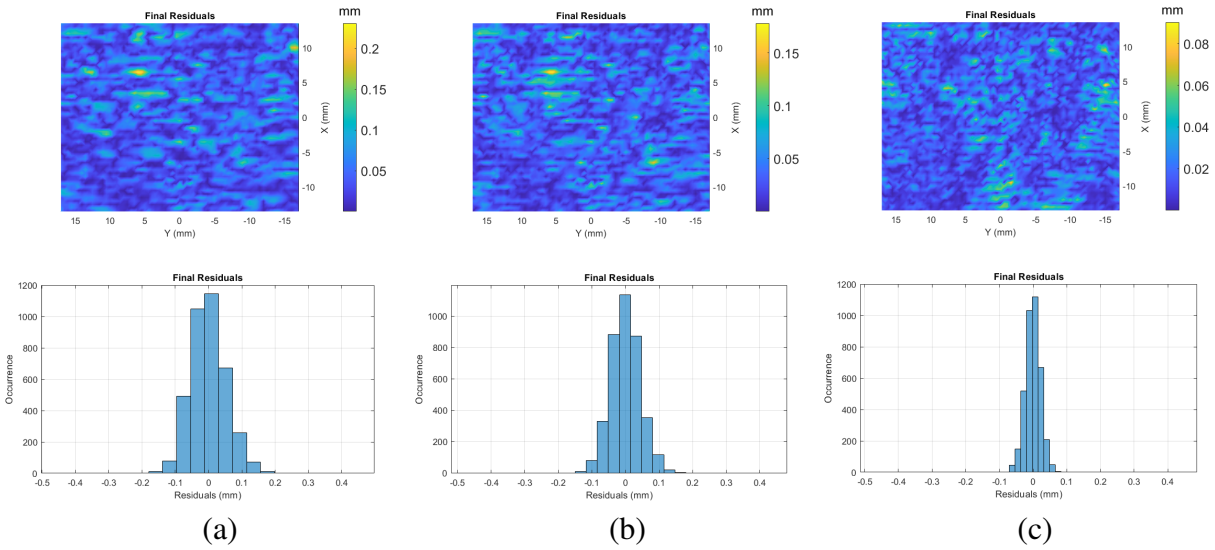

Fig 5 Residuals deviations after the ICP registration using a defect basis of (a) 25, (b) 150, and (c) 850 modes.

scale. The map still shows a homogeneous aspect, indicating that the modeled defects are still at an entity scale.

On the other hand, Fig. 5(c) is closer to representing the geometry deposited during the production. Horizontal stripes, similar to the ones seen on the part in Fig. 2, start to appear but are not totally modeled by the implemented approach. Therefore, higher frequencies and more modes are needed to get, e.g., the first few layers (bottom of the map) and the right side of the part. It is also important to note that the mesh size influences the modeling results as much as the number of modes. A good compromise should be made since bigger mesh will not be able to model bead scale defects, and smaller mesh will be more critical and complicated.

Finally, going to the scale of the beads is interesting and a choice to make in the research work. Moreover, this modal distribution analysis indicates that the estimation done with 25 is enough to measure dimensional and shape defects while increasing the modal basis size will not add remarkable variations to the displacement maps. However, since it does not significantly impact the additive sequence nor the subtractive phase in the case of process hybridization, a modal basis of 25 modes is adapted in the following, and the ATOS Core measurement results (Fig. 4) are used as the reference.

*4.3 **Texture analysis***

In the following, three different textures of the AM surface [Figs. 6(a)-6(c)] are analyzed and compared using the defined criteria in Sec. 2.4. The corresponding regions of interest [Fig. 3(d)] for each texture are shown in the second row of Fig. 6. The conducted analysis on these ROIs evaluates each pattern, especially the natural AM surface, and what it can provide for the image

correlation analysis. It also helps predict and understand measurement results in Sec. 4.4. As shown in Table 2, the average gradient increases with a pattern projection on the natural texture, especially the speckle one. In addition, comparing the three spatial autocorrelation maps (shown in the third row of Fig. 6) shows a clear advantage of the speckle pattern projection. This result can also be seen by comparing the computed autocorrelation RMS, where the third texture presents better results with a value closer to zero (0.051). Self-image comparison with pixel displacements using the regular and well-defined circular pattern leads to similar and contrasting data values, which explains the yellow-blue pattern in Fig. 2(e).

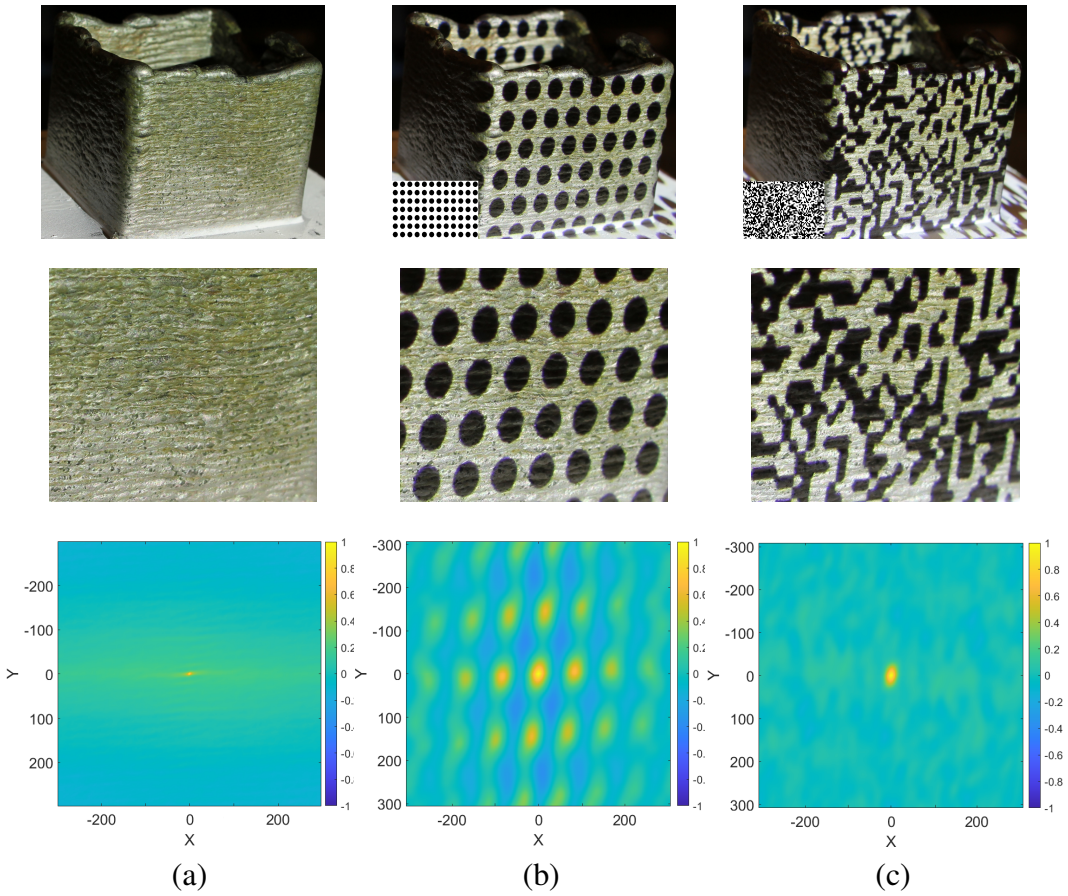

Fig 6 WLAM surface with a highlight on the ROI and its corresponding spatial autocorrelation map with (a) a natural texture, (b) circle, and (c) speckle pattern projection.

Table 2 Image correlation criteria comparison for different textures.

	Natural texture	**Circle Pattern**	**Speckle Pattern**
AG $\left(\mathbf{1/Pixels^2}\right)$	0.055	0.071	0.093
Autocorrelation RMS	0.072	0.210	0.051

*4.4 **Modal stereocorrelation measurements***

First, camera calibration is essential before introducing the measurement results.

4.4.1 Intrinsic calibration

The Canon EOS7D camera's intrinsic parameters are determined using a calibration target presenting a circle pattern. A set of measured points is provided defining the world Points. Therefore, 93 pictures of the target are taken from different angles and positions. Then, centroid points of the circle markers are detected in each image and referred to as image Points. Therefore, having both image and world Points, the camera can be calibrated, and the intrinsic parameters are found.

Hence, a re-projection error is computed by finding the distance between a detected point in a calibration image and its corresponding projected world Point. An overall mean error gives a qualitative measure of accuracy, which is, in the present case, equal to 0.39 pixels. Moreover, the most important thing to check is the standard errors of the estimated camera parameters, which represent their uncertainty (Table 3). Thus, verifying these small errors $\left(\text{magnitudes of } 10^{-2}\right)$, this model can be approved.

Radial and tangential distortions are calculated during this step and removed from the taken part images using the Computer Vision Toolbox in MATLAB. In the following, intrinsic parameters are fixed and used in the remaining steps of the protocol.

Table 3 Canon EOS7D intrinsic parameters.

Focal length (pixels)		**Optical center (pixels)**		**Skew factor**
f_u	f_v	C_{cu}	C_{cv}	s_k
4819.347 $\pm$0.096	4820.482 $\pm$0.098	2577.721 $\pm$0.035	1736.958 $\pm$0.035	1.097 $\pm$0.004

4.4.2 Extrinsic calibration

After fixing the Canon EOS7D intrinsic parameters, left and right pictures of the AM part are used to compute the extrinsic ones. This manufactured column presents remarkable defects, as shown in Fig. 4. That is why the extrinsic calibration steps are based on a powdered substrate with a projected circle pattern. In some cases, the substrate geometry is deformed during AM due to higher generated heat, mainly while producing solid instead of hollow parts. In the following procedure, the shape of the substrate is considered geometrically perfect. In the first step, the nominal 3D meshes of the substrate surfaces, highlighted in Figs. 3(a) and 3(b), are projected on the left and right part images. Then, these meshes are manually aligned by estimating the initial extrinsic parameters. Hence, these previous estimations map the second mesh [Fig. 3(c)] from its

3D frame to image one. A self-calibration calculation based on the image correlation technique follows. Therefore, the extrinsic parameters are optimized to minimize the gray level differences between the images, defined by the correlation residual in Eq. (9). Sixty iterations are needed to converge towards the final solutions using a Levenberg-Marquardt regularization.

4.4.3 Measurements

In the following, stereocorrelation measurements are performed using pair images presenting the three different textures introduced in Sec. 4.3. Therefore, after the optical measurements, the geometrical defects are modeled. The nominal mesh is then deformed using Eq. (10) and the 25 modes basis. At the same time, optimized modal amplitudes are computed to minimize the correlation residual [Eq. (11)]. The convergence of this residual is smoother and almost 20 times faster with pattern texture, as shown in Fig. 7. A better convergence validates the importance and influence of a better image gradient. In the second step, these results are compared to the reference one (ATOS Core measurement). A difference map is obtained by computing the difference between the calculated displacements in each measuring method and for each texture. This map can be presented numerically through the RMS of these displacement differences computed at the end of the optimization (Table 4).

Moreover, having the STD of the differences and the defects' maximum amplitude, a measurement relative error is calculated. All these results show that stereocorrelation measurements are relevant and close to the reference. Hence, the pattern projection advantage was expected, especially the speckle one. The autocorrelation criterion can explain the lower error. In contrast, considering the objective of these defect measurements (updating additive trajectories), the natural texture shows promising results since, in this case, an error of 2.72% is entirely consistent with the requirements of the process.

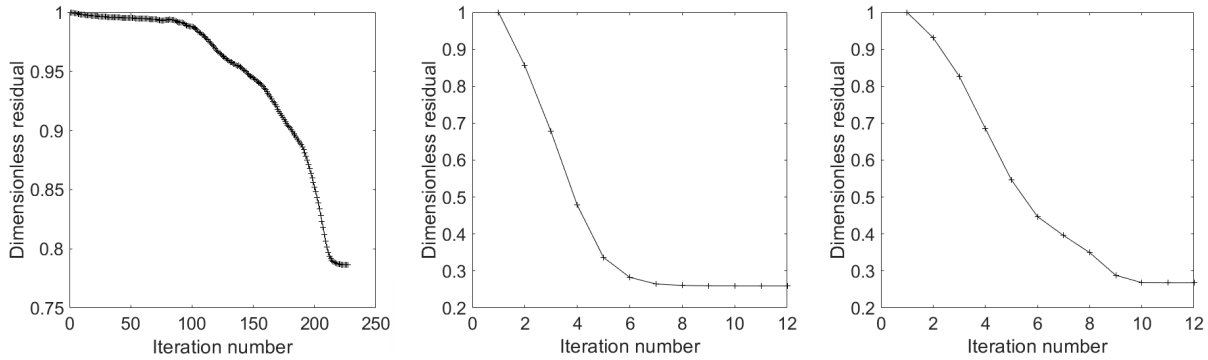

Fig 7 Correlation residual convergence curves using (a) natural texture, (b) circle, and (c) speckle patterns projection.

Table 4 Stereocorrelation measurements compared to the reference ones using different textures.

	Natural texture	**Circle Pattern**	**Speckle Pattern**
Differences with ATOS Core (RMS)	$51.53\mu m$	$35.73\mu m$	$26.3\mu m$
Measurements relative error (%)	2.72	2.22	1.65

The purpose of this comparison is to respond to the goal of this paper; determine the influence of these patterns, and highlight the promising performance of the natural one. In addition, the results explain the link between the measurements and the criteria presented in Table 2 and validate the applicability of this modal stereocorrelation approach in an AM context.

Elements and results from the third texture case are presented next. The pair of images, with speckle pattern projection, used in the stereocorrelation defects measurements is shown in Fig. 8(a). Previously, the residuals convergence curve was presented, whereas Figs. 8(b) and 8(c) shows the corresponding map before and after shape correction. These results give clear information about the correlation residual minimization. Therefore, low and uniform residuals validate the sufficiency of the adapted modal basis in describing the geometrical defects. The shape correction map is visualized separately using the rigid body modes [Fig. 9(a)] and the 22 that follows [Fig. 9(b)]. Figure 9(c) shows their corresponding modal amplitudes distribution.

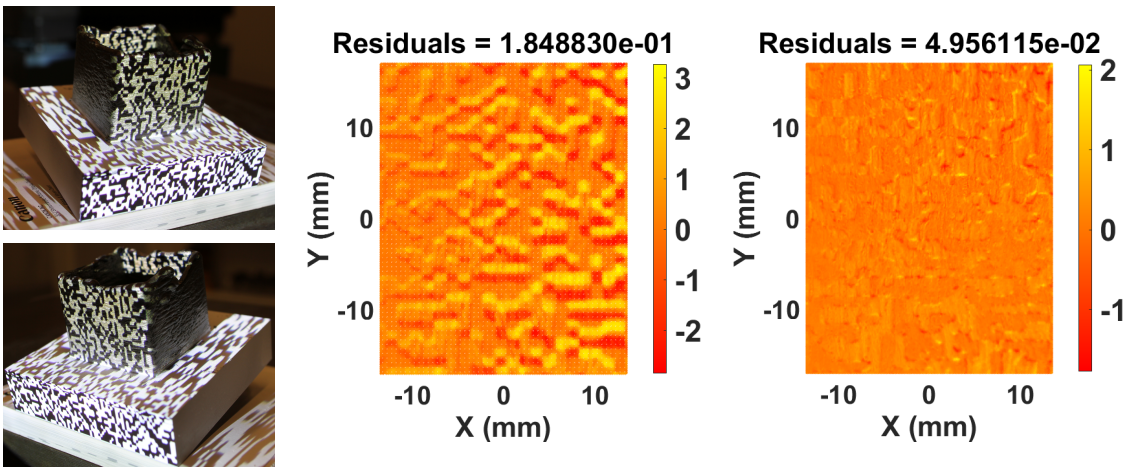

(a) (b) (c)

Fig 8 Pair of images required for (a) the modal stereocorrelation measurement; Correlation residual map (expressed in % of dynamic range) (b) before and (c) after shape correction.

4.5 Measurements repeatability

5 left and 5 right images with speckle pattern projection are used to evaluate measurement repeatability, resulting in 25 possible pairs of images (L1-R1, L1-R2, etc.). These 25 measurements lead

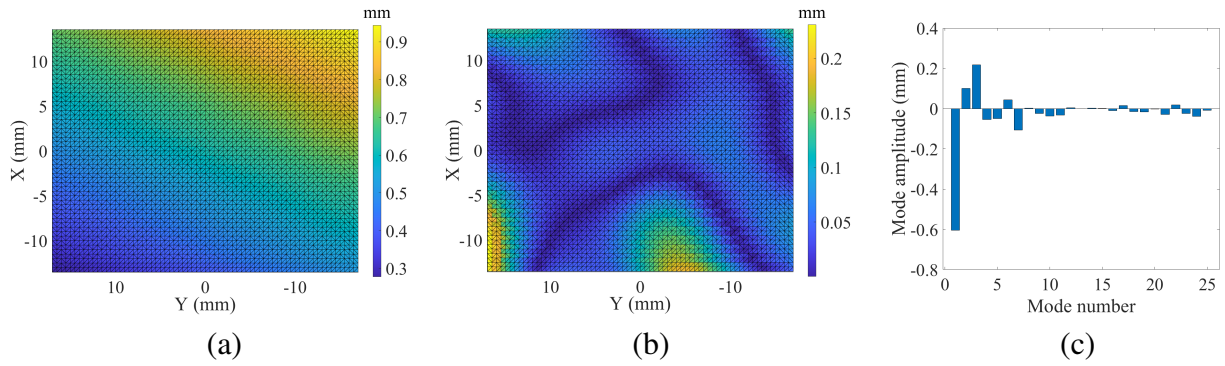

Fig 9 Stereocorrelation measurement results with speckle texture. (a) Geometrical defects measured by three rigid body modes and (b) the following 22, (c) Modal distribution using a 25 modes defect basis.

to average results regarding the correction map and the modal amplitude distribution in addition to their standard deviation. The average modal amplitudes are shown in Fig. 10 with each mode standard deviation regarding these 25 combinations.

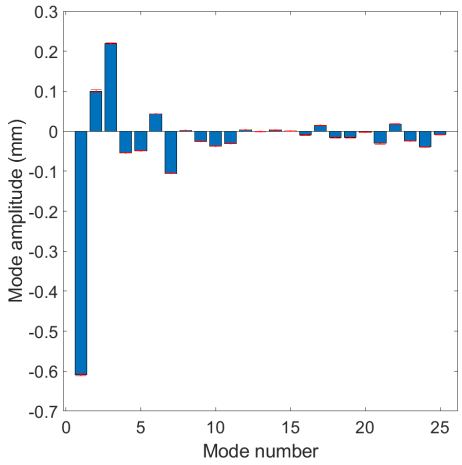

Fig 10 Average modal amplitudes and corresponding error bars (standard deviations).

The maximum error is $3.9\,\mu m$ while the RMS of the 25 deviations is $1.3\,\mu m$. On the other hand, a maximum occurring deviation in the correction maps is $10.9\,\mu m$ while the RMS of the whole deviations is $3.9\,\mu m$. These results again validate this measurement tool (Modal approach based on global stereocorrelation) in estimating geometrical defects in WLAM.

5 Conclusion

This work applies a modal approach based on global stereocorrelation to measure dimensional and shape defects in the WLAM part. A Canon EOS7D camera is used and calibrated by determining its intrinsic and extrinsic parameters separately. Intrinsic parameters are found using a calibration target. In contrast, a self-calibration step computes extrinsic ones based on the part substrate

instead of the measured surface itself due to its remarkable defects. A modal basis of 25 modes is defined, and the stereocorrelation results are compared to defects measured with a reference system (ATOS Core). A 1.65% error compared to the reference system and good measurement repeatability can validate the adapted measurement tool in this research context. It is also important to highlight the pattern projection influence on the measurement results. This texture presents a higher gradient, leading to faster convergence of the correlation residual optimization. In addition, the results obtained with a projected speckle pattern are closer to those measured by the ATOS Core. In contrast, the natural AM texture presented interesting results and sufficient pattern to achieve the measurements.

In future work, an *in-situ* measuring system based on image correlation (CMOS Cameras) will be placed in the hybrid robot cell. A defect base representative of the geometric defects obtained in WLAM processes will be defined on an entity scale. Given this perspective, a technological defect database will be built either by experiments on the process parameters and ATOS Core measurements or by a complete numerical approach. Finally, reconstruction algorithms of a model representing the acquired part geometry with its defects will be developed to realign the additive trajectories and optimize the manufacturing process, which is the primary goal of these upcoming works.

Disclosures

The authors declare that they have no known competing financial interests or personal relationships that could have appeared to influence the work reported in this paper.

Data Availability

Data will be made available on request. All of the experimental results in our manuscript are obtained from experiments.

Acknowledgments

This work was part of the AWESOME project and is supported by a grant overseen by the French National Research Agency (ANR-21-CE10-0013). The authors gratefully acknowledge the technical support provided by the Paris-Saclay AM Platform funded by Université Paris- Saclay and École normale supérieure Paris-Saclay through the strategic research initiative program (ANR-11-IDEX-0003-02).

References

1 X. Chen, F. Kong, Y. Fu, *et al.*, "A review on wire-arc additive manufacturing: typical defects, detection approaches, and multisensor data fusion-based model," *The International Journal of Advanced Manufacturing Technology* **117**(3-4), 707–727 (2021).

2 D. Svetlizky, M. Das, B. Zheng, *et al.*, "Directed energy deposition (DED) additive manufacturing: Physical characteristics, defects, challenges and applications," *Materials Today* **49**, 271–295 (2021).

3 M. Grasso and B. M. Colosimo, "Process defects and *in situ* monitoring methods in metal powder bed fusion: a review," *Measurement Science and Technology* **28**(4), 044005 (2017).

4 B. Wu, Z. Pan, D. Ding, *et al.*, "A review of the wire arc additive manufacturing of metals: properties, defects and quality improvement," *Journal of Manufacturing Processes* **35**, 127–139 (2018).

5 M. Shaloo, M. Schnall, T. Klein, *et al.*, "A review of non-destructive testing (NDT) techniques for defect detection: application to fusion welding and future wire arc additive manufacturing processes," *Materials* **15**(10), 3697 (2022).

6 M. Liu, A. Kumar, S. Bukkapatnam, *et al.*, "A review of the anomalies in directed energy deposition (DED) processes & potential solutions - part quality & defects," *Procedia Manufacturing* **53**, 507–518 (2021).

7 D. Etievant, Y. Quinsat, F. Thiebaut, *et al.*, "A modal approach for shape defect measurement based on global stereocorrelation," *Optics and Lasers in Engineering* **128**, 106030 (2020).

8 G. Rebergue, B. Blaysat, H. Chanal, *et al.*, "In-situ measurement of machining part deflection with Digital Image Correlation," *Measurement* **187**, 110301 (2022).

9 L. Dubreuil, *Mesure In-situ par moyens optiques*. PhD thesis, Université Paris-Saclay (2017).

10 J.-E. Dufour, *Mesures de forme, de déplacement, et de paramètres mécaniques parstéréocorrélation d'images isogéométrique*. PhD thesis, Université Paris-Saclay (2015).

11 F. Thiébaut, S. Bendjebla, Y. Quinsat, *et al.*, "Nonrigid registration for form defect identification of thin parts," *Journal of Computing and Information Science in Engineering* **18**(2), 021012 (2018).

12 B. Beaubier, J.-E. Dufour, F. Hild, *et al.*, "CAD-based calibration and shape measurement with stereoDIC: Principle and application on test and industrial parts," *Experimental Mechanics* **54**(3), 329–341 (2014).

13 L. Dubreuil, J.-E. Dufour, Y. Quinsat, *et al.*, "Mesh-Based Shape Measurements with Stereocorrelation: Principle and First Results," *Experimental Mechanics* **56**(7), 1231–1242 (2016).

14 G. Bomarito, J. Hochhalter, T. Ruggles, *et al.*, "Increasing accuracy and precision of digital image correlation through pattern optimization," *Optics and Lasers in Engineering* **91**, 73–85 (2017).

15 M. Grédiac, B. Blaysat, and F. Sur, "On the optimal pattern for displacement field measurement: Random speckle and DIC, or checkerboard and LSA?," *Experimental Mechanics* **60**(4), 509–534 (2020).

16 P. L. Reu, B. Blaysat, E. Andó, *et al.*, "DIC challenge 2.0: Developing images and guidelines for evaluating accuracy and resolution of 2d analyses: Focus on the metrological efficiency indicator," *Experimental Mechanics* **62**(4), 639–654 (2022).

17 J. Heikkila and O. Silven, "A four-step camera calibration procedure with implicit image correction," in *Proceedings of IEEE Computer Society Conference on Computer Vision and Pattern Recognition*, 1106–1112, IEEE Comput. Soc (1997).

18 J. Salvi, X. Armangué, and J. Batlle, "A comparative review of camera calibrating methods with accuracy evaluation," *Pattern Recognition* **35**(7), 1617–1635 (2002).

19 Z. Zhang, "A flexible new technique for camera calibration," *IEEE Transactions on Pattern Analysis and Machine Intelligence* **22**(11), 1330–1334 (2000).

20 D. Etievant, *Une approche unifiée pour la mesure et l'analyse des défauts de forme des pièces mécaniques*. PhD thesis, Université Paris-Saclay (2022).

21 C. Zhao, Z. Wang, H. Li, *et al.*, "A new approach for medical image enhancement based on luminance-level modulation and gradient modulation," *Biomedical Signal Processing and Control* **48**, 189–196 (2019).

Khalil Hachem is a PhD student in the University Research Laboratory in Automated Production (LURPA) at ENS Paris-Saclay, France. His research focuses on updating the geometric model produced in additive manufacturing by measuring *in-situ* the part and modeling its defects. He earned his bachelor's degree in Mechanical engineering from the Lebanese University Faculty of Engineering in 2022. He received his master's 2 in advanced manufacturing and smart systems from the Paris-Saclay University, France, in 2022.

Yann Quinsat is an assistant professor at ENS Paris Saclay. After obtaining his PhD from Blaise Pascal University (France), he has been teaching mechanical engineering at ENS Paris Saclay since 2004. He is currently working on manufacturing processes (hybrid manufacturing) and, in particular, the development of *in-situ* measurement operations using contactless sensors associated to process correction.

Christophe Tournier received his PhD in manufacturing engineering from ENS Cachan (Paris, France) in 2001. From 2011, he is professor at the Department of Mechanical Engineering of the ENS Paris-Saclay, and at the Graduate School of Engineering and Systems Sciences at the Paris-Saclay University (France). He was a visiting scientist at EPFL (Switzerland) from September 2010 to July 2011. His research focuses on advanced manufacturing including CAD/CAM, 5-axis machining and polishing, additive manufacturing, CNC design, and machine tool behavior.

Nicolas Béraud obtained his PhD in metal additive manufacturing from Grenoble Alpes University in 2016. Since 2019, he has been teaching mechanical engineering at Grenoble Alpes University and doing his research on improving metal additive processes, particularly from a thermal point of view.